8. Electronic Properties of Semiconductor Interfaces

In this chapter we investigate the electronic properties of semiconductor interfaces. Semiconductor devices contain metal–semiconductor, insulator–semiconductor, insulator–metal and/or semiconductor–semiconductor interfaces. The electronic properties of these interfaces determine the characteristics of the device. The band structure lineup at all these interfaces is determined by one unifying concept, the continuum of interface-induced gap states (IFIGS). These intrinsic interface states are the wave-function tails of electron states that overlap the fundamental band gap of a semiconductor at the interface; in other words they are caused by the quantum-mechanical tunneling effect. IFIGS theory quantitatively explains the experimental barrier heights of well-characterized metal–semiconductor or Schottky contacts as well as the valence-band offsets of semiconductor–semiconductor interfaces or semiconductor heterostructures. Insulators are viewed as semiconductors with wide band gaps.

In his pioneering article entitled *Semiconductor Theory of the Blocking Layer*, *Schottky* [8.1] finally explained the rectifying properties of metal–semiconductor contacts, which had first been described by *Braun* [8.2], as being due to a depletion of the majority carriers on the semiconductor side of the interface. This new depletion-layer concept immediately triggered a search for a physical explanation of the barrier heights observed in metal–semiconductor interfaces, or Schottky contacts as they are also called in order to honor Schottky's many basic contributions to this field.

The early Schottky–Mott rule [8.3, 4] proposed that n-type (p-type) barrier heights were equal to the difference between the work function of the metal and the electron affinity (ionization energy) of the semiconductor. A plot of the experimental barrier heights of various metal–selenium rectifiers versus the work functions of the corresponding metals did indeed reveal a linear correlation, but the slope parameter was much smaller than unity [8.4]. To resolve the failure of the very simple and therefore attractive Schottky–Mott rule, *Bardeen* [8.5] proposed that electronic interface states in the semiconductor band gap play an essential role in the charge balance at metal–semiconductor interfaces.

Heine [8.6] considered the quantum-mechanical tunneling effect at metal–semiconductor interfaces and noted that *for energies in the semiconductor band gap, the volume states of the metal have tails in the semiconductor*. *Tejedor* and *Flores* [8.7] applied this same idea to semiconductor heterostructures where, for energies in the band-edge discontinuities, the volume states of one semiconductor tunnel into the other. The continua of interface-induced gap states (IFIGS), as these evanescent states were later called, are an intrinsic property of semiconductors and they are the *fundamental* physical mechanism that determines the band-structure lineup at both metal–semiconductor contacts and semiconductor heterostructures: in other words, at all semiconductor interfaces. Insulator interfaces are also included in this, since insulators may be described as wide-gap semi-
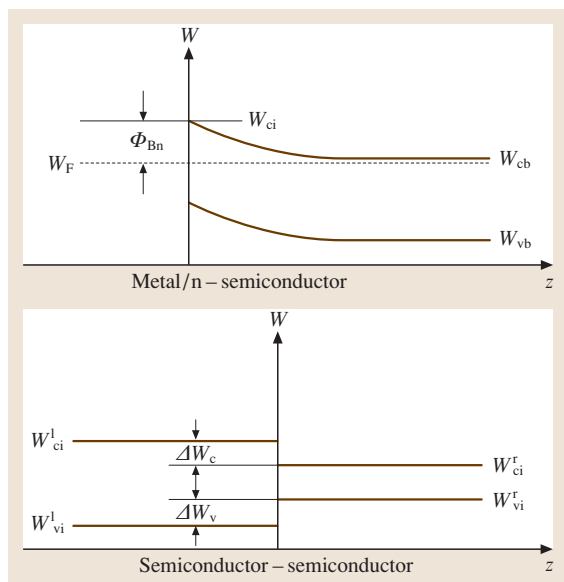
Fig. 8.1 Schematic energy-band diagrams of metal–semiconductor contacts and semiconductor heterostructures. W_F: Fermi level; Φ_{Bn}: barrier height; W_v and W_c: valence-band maximum and conduction-band minimum, respectively; ΔW_v and ΔW_c: valence- and conduction-band offset, respectively; i and b: values at the interface and in the bulk, respectively; r and l: right and left side, respectively

conductors. Figure 8.1 shows schematic band diagrams of an n-type Schottky contact and a semiconductor heterostructure.

The IFIGS continua derive from both the valence- and the conduction-band states of the semiconductor. The energy at which their predominant character changes from valence-band-like to conduction-band-like is called their branch point. The position of the Fermi level relative to this branch point then determines the sign and the amount of the net charge in the IFIGS. Hence, the IFIGS give rise to intrinsic interface dipoles. Both the barrier heights of Schottky contacts and the band offsets of heterostructures thus divide up into a zero-charge-transfer term and an electric-dipole contribution.

From a more chemical point of view, these interface dipoles may be attributed to the partial ionic character of the covalent bonds between atoms right at the interface. Generalizing *Pauling's* [8.8] electronegativity concept,

the difference in the electronegativities of the atoms involved in the interfacial bonds also describes the charge transfer at semiconductor interfaces. Combining the physical IFIGS and the chemical electronegativity concept, the electric-dipole contributions of Schottky barrier heights as well as those of heterostructure band offsets vary proportional to the difference in the electronegativities of the metal and the semiconductor and of the two semiconductors, respectively. The electronegativities of the Group IV elemental and the IV–IV, III–V, and II–VI compound semiconductors are almost equal, since the elements that constitute these semiconductors are all placed in the middle of the Periodic Table. Hence, the IFIGS dipole terms of the respective semiconductor heterostructures will be small and may be neglected [8.9]. The valence-band offsets of nonpolar, of lattice-matched and of metamorphic heterostructures should thus equal the difference between the branch-point energies of the semiconductors in contact.

The theoreticians appreciated *Heine*'s IFIGS concept at once. The initial reluctance of most experimentalists was motivated by the observation that the predictions of the IFIGS theory only marked upper limits for the barrier heights observed with *real* Schottky contacts [8.10]. *Schmitsdorf* et al. [8.11] finally resolved this dilemma. They found a linear decrease in the effective barrier height with increasing ideality factors for their Ag/n-Si(111) diodes. Such behavior has been observed for all of the Schottky contacts investigated so far. *Schmitsdorf* et al. attributed this correlation to patches of decreased barrier heights and lateral dimensions smaller than the depletion layer width [8.12]. Consequently, they extrapolated their plots of effective barrier height versus ideality factor to the ideality factor determined by the image-force or Schottky effect [8.13] alone; in this way, they obtained the barrier heights of the laterally homogeneous contacts. The barrier heights of laterally uniform contacts can also be determined from capacitance–voltage measurements (C/V) and by applying ballistic-electron-emission microscopy (BEEM) and internal photoemission yield spectroscopy (IPEYS). The I/V, C/V, BEEM, and IPEYS data agree within the margins of experimental error.

Mönch [8.14] found that the barrier heights of laterally homogeneous Schottky contacts as well as the experimentally observed valence band offsets of semiconductor heterostructures agree excellently with the predictions of the IFIGS-and-electronegativity theory.

8.1 Experimental Database

8.1.1 Barrier Heights of Laterally Homogeneous Schottky Contacts

I/V Characteristics

The current transport in real Schottky contacts occurs via thermionic emission over the barrier provided the doping level of the semiconductor is not too high [8.15]. For doping levels larger than approximately 10^{18} per cm^3, the depletion layer becomes so narrow that tunnel or field emission through the depletion layer prevails. The current–voltage characteristics then become ohmic rather than rectifying.

For thermionic emission over the barrier, the current–voltage characteristics may be written as (see, for example, [8.14])

$$I_{te} = A A_R^* T^2 \exp\left(-\Phi_{Bn}^{eff}/k_B T\right) \exp(e_0 V_c/n k_B T)$$
$$\times [1 - \exp(-e_0 V_c/k_B T)] , \qquad (8.1)$$

where A is the diode area, A_R^* is the effective Richardson constant of the semiconductor, and k_B, T, and e_0 are Boltzmann's constant, the temperature, and the electronic charge, respectively. The effective Richardson constant is defined as

$$A_R^* = \frac{4\pi e_0 k_B m_n^*}{h^3} = A_R \frac{m_n^*}{m_0} , \qquad (8.2)$$

where $A_R = 120\,\mathrm{A\,cm^{-2}\,K^{-2}}$ is the Richardson constant for thermionic emission of nearly free electrons into vacuum, h is Planck's constant, and m_0 and m_n^* are the vacuum and the effective conduction-band mass of electrons, respectively. The externally applied bias V_a divides up into a voltage drop V_c across the depletion layer of the Schottky contact and an *IR* drop at the series resistance R_s of the diode, so that $V_c = V_a - IR_s$. For *ideal* (intimate, abrupt, defect-free, and, above all, laterally homogeneous) Schottky contacts, the effective zero-bias barrier height Φ_{Bn}^{eff} equals the difference $\Phi_{Bn}^{hom} - \delta\Phi_{if}^0$ between the homogeneous barrier height and the zero-bias image-force lowering (see [8.14])

$$\delta\Phi_{if}^0 = e_0 \left[\frac{2e_0^2 N_d}{(4\pi)^2 \varepsilon_\infty^2 \varepsilon_b \varepsilon_0^3} \left(e_0 \left| V_i^0 \right| - k_B T \right) \right]^{1/4} , \qquad (8.3)$$

where N_d is the donor density, $e_0|V_i^0|$ is the zero-bias band bending, ε_∞ and ε_b are the optical and the bulk dielectric constant, respectively, and ε_0 is the permittivity

of vacuum. The ideality factor n describes the voltage dependence of the barrier height and is defined by

$$1 - 1/n = \partial\Phi_{Bn}^{eff}/\partial e_0 V_c . \qquad (8.4)$$

For *real* diodes, the ideality factors n are generally found to be larger than the ideality factor

$$n_{if} = \left(1 - \frac{\delta\Phi_{if}^0}{4e_0|V_i^0|} \right)^{-1} , \qquad (8.5)$$

which is determined by the image-force effect only.

The effective barrier heights and the ideality factors of real Schottky diodes fabricated under experimentally identical conditions vary from one specimen to the next. However, the variations of both quantities are correlated, and the Φ_{Bn}^{eff} values become smaller as the ideality factors increase. As an example, Fig. 8.2 displays Φ_{Bn}^{eff} versus n data for Ag/n-Si(111) contacts with $(1 \times 1)^i$- unreconstructed and $(7 \times 7)^i$-reconstructed interfaces [8.11]. The dashed and dash-dotted lines are the linear least-squares fits to the data points. The linear dependence of the effective barrier height on the ideality factor may be written as

$$\Phi_{Bn}^{eff} = \Phi_{Bn}^{nif} - \varphi_p(n - n_{if}) , \qquad (8.6)$$

where Φ_{Bn}^{nif} is the barrier height at the ideality factor n_{if}. Several conclusions may be drawn from this relation. First, the $\Phi_{Bn}^{eff} - n$ correlation shows that more than
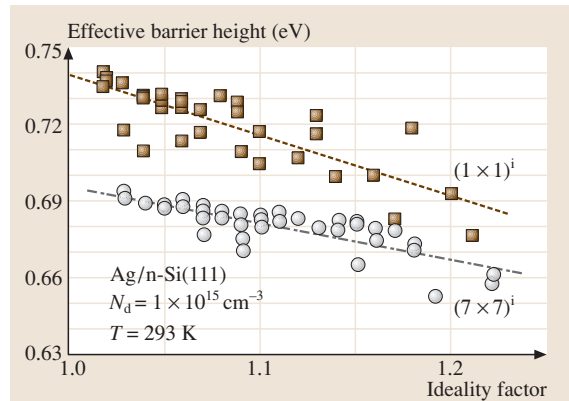

Fig. 8.2 Effective barrier heights versus ideality factors determined from *I/V* characteristics of Ag/n-Si(111)-$(7 \times 7)^i$ and -$(1 \times 1)^i$ contacts at room temperature. The *dashed* and *dash-dotted* lines are the linear least-squares fits to the data. After [8.11]

one physical mechanism determines the barrier heights of *real* Schottky contacts. Second, the extrapolation of Φ_{Bn}^{eff} versus n curves to n_{if} removes all mechanisms that cause a larger bias dependence of the barrier height than the image-force effect itself from consideration. Third, the extrapolated barrier heights Φ_{Bn}^{nif} are equal to the zero-bias barrier height $\Phi_{Bn}^{hom} - \delta\Phi_{if}^{0}$ of the laterally homogeneous contact.

The laterally homogeneous barrier heights obtained from Φ_{Bn}^{eff} versus n curves to n_{if} are not necessarily characteristic of the corresponding *ideal* contacts. This is illustrated by the two data sets displayed in Fig. 8.2, which differ in the interface structures of the respective diodes. Quite generally, structural rearrangements such as the $(7\times7)^{i}$ reconstruction are connected with a redistribution of the valence charge. The bonds in perfectly ordered bulk silicon, the example considered here, are purely covalent, and so reconstructions are accompanied by electric $Si^{+\Delta q}-Si^{-\Delta q}$ dipoles. The $Si(111)$-(7×7) reconstruction is characterized by a stacking fault in one half of its unit mesh [8.16]. *Schmitsdorf* et al. [8.11] quantitatively explained the experimentally observed reduction in the laterally homogeneous barrier height of the $(7\times7)^{i}$ with regard to the $(1\times1)^{i}$ diodes by the electric dipole associated with the stacking fault of the $Si(111)$-7×7 reconstruction.

Patches of reduced barrier height with lateral dimensions smaller than the depletion layer width that are embedded in large areas of laterally homogeneous barrier height is the only known model that explains a lowering of effective barrier heights with increasing ideality factors. In their phenomenological studies of such patchy Schottky contacts, *Freeouf* et al. [8.12] found that the potential distribution exhibits a saddle point in front of such nanometer-size patches of reduced barrier height. Figure 8.4 explains this behavior. The saddle-point barrier height strongly depends on the voltage drop V_{c} across the depletion layer. *Freeouf* et al. simulated the current transport in such patchy Schottky contacts and found a reduction in the effective barrier height and a correlated increase in the ideality factor as they reduced the lateral dimensions of the patches. However, they overlooked the fact that the barrier heights of the laterally homogeneous contacts may be obtained from Φ_{Bn}^{eff} versus n plots, by extrapolating to n_{if}.

C/V Characteristics

Both the space charge and the width of the depletion layers at metal–semiconductor contacts vary as a function of the externally applied voltage. The space-charge the-
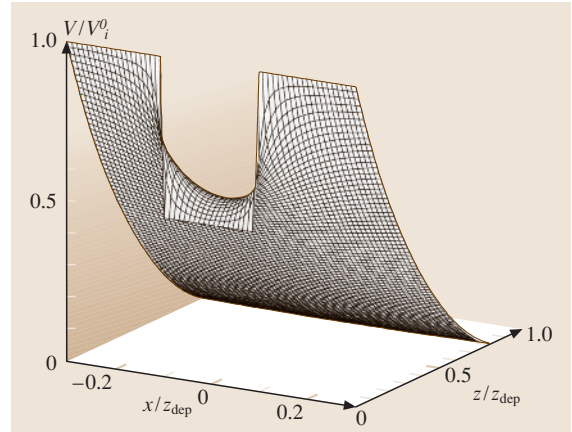

Fig. 8.3 Calculated potential distribution underneath and around a patch of reduced interface potential embedded in a region of larger interface band-bending. The lateral dimension and the interface potential reduction of the patch are set to two tenths of the depletion layer width z_{dep} and one half of the interface potential of the surrounding region

ory gives the variation in the depletion layer capacitance per unit area as (see [8.14])

$$C_{dep} = \left\{ e_0^2 \varepsilon_b \varepsilon_0 N_d / 2 \left[e_0 \left(|V_i^0| - V_c \right) - k_B T \right] \right\}^{1/2} . \tag{8.7}$$

The current through a Schottky diode biased in the reverse direction is small, so the *IR* drop due to the series resistance of the diode may be neglected. Consequently, the extrapolated intercepts on the abscissa of $1/C_{dep}^2$ versus V_a plots give the band bending $e_0|V_i^0|$ at the interface, and together with the energy distance $W_n = W_F - W_{cb}$ from the Fermi level to the conduction band minimum in the bulk, one obtains the flat-band barrier height $\Phi_{Bn}^{fb} \equiv \Phi_{Bn}^{hom} = e_0|V_i^0| + W_n$ which equals the laterally homogeneous barrier height of the contact.

As an example, Fig. 8.4 displays the flat-band barrier heights of the same Ag/n-$Si(111)$ diodes that are discussed in Fig. 8.2. The dashed and dash-dotted lines are the Gaussian least-squares fits to the data from the diodes with $(1\times1)^{i}$ and $(7\times7)^{i}$ interface structures, respectively. Within the margins of experimental error the peak C/V values agree with the laterally homogeneous barrier heights obtained from the extrapolations of the I/V data shown in Fig. 8.2. These data clearly demonstrate that barrier heights characteristic of laterally homogeneous Schottky contacts can be only obtained from I/V or C/V data from many diodes fabricated under identical conditions rather than from a single diode. However, the
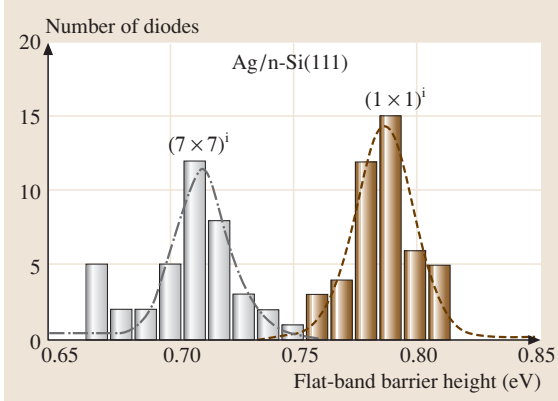
Fig. 8.4 Histograms of flat-band barrier heights determined from C/V characteristics of Ag/n-Si(111)-$(7 \times 7)^i$ and -$(1 \times 1)^i$ contacts at room temperature. The data were obtained with the same diodes discussed in Fig. 8.2. The *dashed* and *dash-dotted lines* are the Gaussian least-squares fits to the data. After [8.11]

Fig. 8.5 Histograms of local BEEM barrier heights of two Pd/n-6H-SiC(0001) diodes with ideality factors of 1.06 (*gray solid bars*) and 1.49 (*empty bars*). The data were obtained by fitting the square law (8.8) to 800 BEEM I_{coll}/V_{tip} spectra each. Data from *Im* et al. [8.17]

effective barrier heights and the ideality factors vary as a function of the diode temperature. Hence, effective barrier heights and ideality factors evaluated from the I/V characteristics for one and the same diode recorded at different temperatures are also suitable for determining the corresponding laterally homogeneous barrier height (see [8.14]).

Ballistic–Electron–Emission Microscopy

In ballistic-electron-emission microscopy (BEEM) [8.18], a tip injects almost monoenergetic electrons into the metal film of a Schottky diode. These tunnel-injected electrons reach the semiconductor as ballistic electrons provided that they lose no energy on their way through the metal. Hence, the collector current I_{coll} is expected to set in when the ballistic electrons surpass the metal–semiconductor barrier; in other words, if the voltage V_{tip} applied between tip and metal film exceeds the *local* potential barrier $\Phi_{Bn}^{loc}(z)/e_0$. *Bell* and *Kaiser* [8.19] derived the square law

$$I_{coll}(z) = R^* I_{tip} \left[e_0 V_{tip} - \Phi_{Bn}^{loc}(z) \right]^2 \tag{8.8}$$

for the BEEM I_{coll}/V_{tip} characteristics, where I_{tip} is the injected tunnel current. BEEM measures *local* barrier heights; most specifically, the saddle-point barrier heights in front of nanometer-sized patches rather than their lower barrier heights right at the interface.

BEEM is *the* experimental tool for measuring spatial variations in the barrier height on the nanometer-scale.
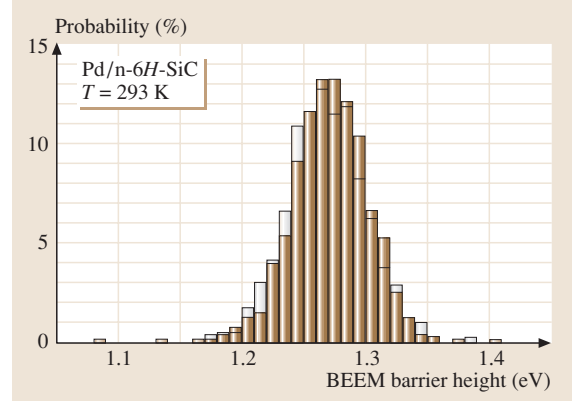
The local barrier heights are determined by fitting relation (8.8) to measured I_{coll}/V_{tip} characteristics recorded at successive tip positions along lateral line scans. Figure 8.5 displays histograms of the local BEEM barrier heights of two Pd/n-6H-SiC(0001) diodes [8.17]. The diodes differ in their ideality factors, 1.06 and 1.49, which are close to and much larger, respectively, than the value $n_{if} = 1.01$ determined solely by the image-force effect. Obviously, the *nanometer-scale* BEEM histograms of the two diodes are identical although their *macroscopic* ideality factors and therefore their patchinesses differ. Two important conclusions were drawn from these findings. First, these data suggest the existence of two different types of patches, intrinsic and extrinsic ones. The intrinsic patches might be correlated with the random distributions of the ionized donors and acceptors which cause nanometer-scale lateral fluctuations in the interface potential. A few gross interface defects of extrinsic origin, which escape BEEM observations, are then responsible for the variations in the ideality factors. Second, Gaussian least-squares fits to the histograms of the local BEEM barrier heights yield peak barrier heights of 1.27 ± 0.03 eV. Within the margins of experimental error, this value agrees with the laterally homogeneous value of 1.24 ± 0.09 eV which was obtained by extrapolation of the linear least-squares fit to a Φ_{Bn}^{eff} versus n plot to n_{if}. The nanometer-scale BEEM histograms and the macroscopic I/V characteristics thus provide identical barrier heights of laterally homogeneous Schottky contacts.

Internal Photoemission Yield Spectroscopy

Metal-semiconductor contacts show a photoelectric response to optical radiation with photon energies smaller than the width of the bulk band gap. This effect is caused by photoexcitation of electrons from the metal over the interfacial barrier into the conduction band of the semiconductor. Experimentally, the internal photoemission yield, which is defined as the ratio of the photoinjected electron flux across the barrier into the semiconductor to the flux of the electrons excited in the metal, is measured as a function of the energy of the incident photons. Consequently, this technique is called internal photoemission yield spectroscopy (IPEYS). *Cohen* et al. [8.21] derived that the internal photoemission yield varies as a function of the photon energy $\hbar\omega$ as

$$Y(\hbar\omega) \propto \left(\hbar\omega - \Phi_{\mathrm{Bn}}^{\mathrm{IPEYS}}\right)^2 \Big/ \hbar\omega . \tag{8.9}$$

Patches only cover a small portion of the metal–semiconductor interface, so the threshold energy $\Phi_{\mathrm{Bn}}^{\mathrm{IPEYS}}$ will equal the barrier height $\Phi_{\mathrm{Bn}}^{\mathrm{hom}}$ of the laterally homogeneous part of the contact minus the zero-bias image-force lowering $\delta\Phi_{\mathrm{if}}^0$.

In Fig. 8.6, experimental $[Y(\hbar\omega) \cdot \hbar\omega]^{1/2}$ data for a Pt/p-Si(001) diode [8.20] are plotted versus the energy of the exciting photons. The dashed line is the linear least-squares fit to the data. The deviation of the experimental $[Y(\hbar\omega) \cdot \hbar\omega]^{1/2}$ data towards larger values slightly below and above the threshold is caused by the shape of the Fermi–Dirac distribution function at finite temperatures and by the existence of patches with barrier heights smaller and larger than $\Phi_{\mathrm{Bn}}^{\mathrm{hom}}$.

8.1.2 Band Offsets of Semiconductor Heterostructures

Semiconductors generally grow layer-by-layer, at least initially. Hence, core-level photoemission spectroscopy (PES) is a very reliable tool and the one most widely used to determine the band-structure lineup at semiconductor heterostructures. The valence-band offset may be obtained from the energy positions of core-level lines in X-ray photoelectron spectra recorded with bulk samples of the semiconductors in contact and with the interface itself [8.22]. Since the escape depths of the photoelectrons are on the order of just 2 nm, one of the two semiconductors must be sufficiently thin. This condition is easily met when heterostructures are grown by molecular beam epitaxy (MBE) and PE spectra are recorded during growth interrupts.
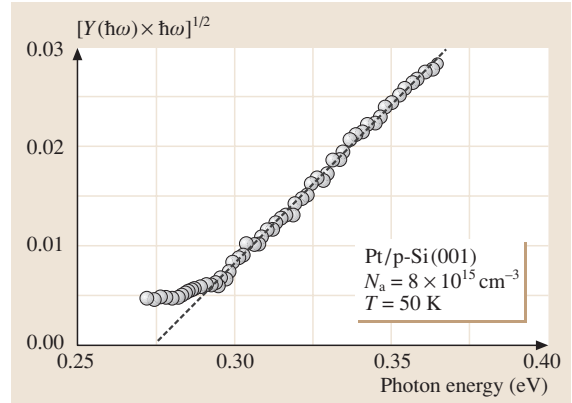
Fig. 8.6 Spectral dependence of the internal photoemission yield $\sqrt{Y(\hbar\omega) \cdot \hbar\omega}$ of a Pt/p-Si(001) diode versus photon energy of the exciting light. The *dashed line* is the linear least-squares fit to the data for photon energies larger than 0.3 eV. Data from *Turan* et al. [8.20]

The valence-band discontinuity is then given by (see Fig. 8.7)

$$\begin{aligned}\Delta W_{\mathrm{v}} &= W_{\mathrm{vir}} - W_{\mathrm{vil}} = W_{\mathrm{i}}(\mathrm{n_r}l_r) - W_{\mathrm{i}}(\mathrm{n_l}l_l) \\ &+ [W_{\mathrm{vbr}} - W_{\mathrm{b}}(\mathrm{n_r}l_r)] - [W_{\mathrm{vbl}} - W_{\mathrm{b}}(\mathrm{n_l}l_l)] ,\end{aligned} \tag{8.10}$$

where $\mathrm{n_r}l_r$ and $\mathrm{n_l}l_l$ denote the core levels of the semiconductors on the right (r) and the left (l) side of the interface, respectively. The subscripts i and b characterize interface and bulk properties, respectively. The
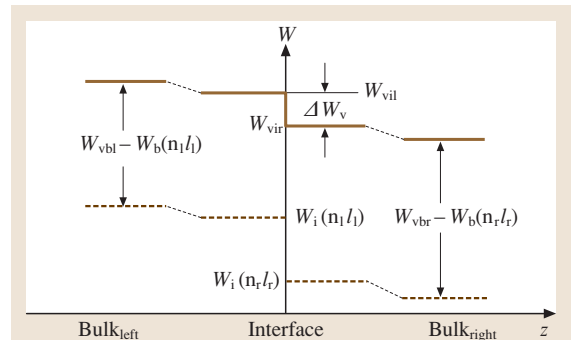
Fig. 8.7 Schematic energy band diagram at semiconductor heterostructures. W_{vb} and W_{vi} are the valence-band maxima and $W_{\mathrm{b}}(nl)$ and $W_{\mathrm{i}}(nl)$ are the core levels in the bulk and at the interface, respectively. The subscripts l and r denote the semiconductors on the right and the on the left side of the interface. ΔW_{v} is the valence-band offset. The *thin dashed lines* account for possible band-bending from space-charge layers

energy difference $W_i(n_r l_r) - W_i(n_l l_l)$ between the core levels of the two semiconductors at the interface is determined from energy distribution curves of photoelectrons recorded during MBE growth of the heterostructure. The energy positions $W_{vbr} - W_b(n_r l_r)$ and $W_{vbl} - W_b(n_l l_l)$ of the core levels relative to the valence-band maxima in the bulk of the two semiconductors are evaluated separately.

Another widely used technique for determining band offsets in heterostructures is internal photoemission yield spectroscopy. The procedure for evaluating the IPEYS signals is the same as described in Sect. 8.1.1.

8.2 IFIGS–and–Electronegativity Theory

Because of the quantum-mechanical tunneling effect, the wavefunctions of bulk electrons decay exponentially into vacuum at surfaces or, more generally speaking, at solid–vacuum interfaces. A similar behavior occurs at interfaces between two solids [8.6, 7]. In energy regions of Schottky contacts and semiconductor heterostructures where occupied band states overlap a band gap, the wavefunctions of these electrons will tail across the interface. The only difference to solid–vacuum interfaces is that the wavefunction tails oscillate at solid–solid interfaces. Figure 8.8 schematically explains the tailing effects at surfaces and semiconductor interfaces. For the band-structure lineup at semiconductor interfaces, only the tailing states within the gap between the top valence and the lowest conduction band are of any real importance since the energy position of the Fermi level determines their charging state. These wavefunction tails or interface-induced gap states (IFIGS) derive from the continuum of the virtual gap states (ViGS) of the complex semiconductor band structure. Hence, the IFIGS are an intrinsic property of the semiconductor.

The IFIGS are made up of valence-band and conduction-band states of the semiconductor. Their net charge depends on the energy position of the Fermi level relative to their branch point, where their character changes from predominantly donor- or valence band-like to mostly acceptor- or conduction band-like. The band-structure lineup at semiconductor interfaces is thus described by a zero-charge-transfer term and an electric dipole contribution.

In a more chemical approach, the charge transfer at semiconductor interfaces may be related to the partly ionic character of the covalent bonds at interfaces. *Pauling* [8.8] described the ionicity of single bonds in diatomic molecules by the difference between the electronegativities of the atoms involved. The binding energies of core-level electrons are known to depend on the chemical environment of the atoms or, in other words, on the ionicity of their chemical bonds. Figure 8.9 displays experimentally observed chemical shifts for Si(2p) and Ge(3d) core levels induced by metal adatoms
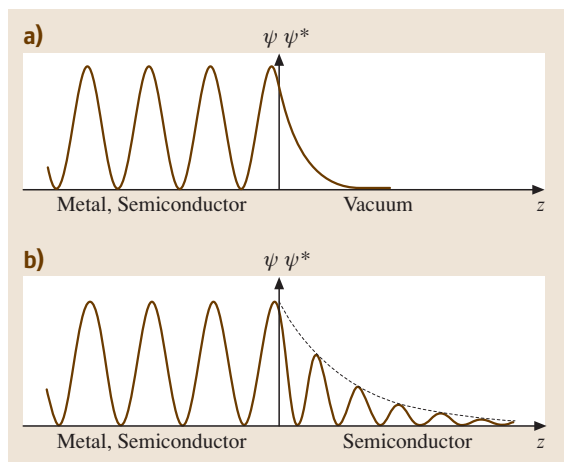

Fig. 8.8a,b Wavefunctions at clean surfaces (**a**) and at metal–semiconductor and semiconductor–semiconductor interfaces (**b**) (schematically)
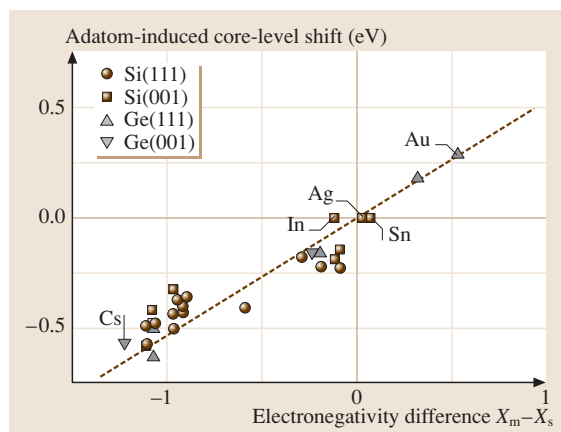

Fig. 8.9 Chemical shifts of Si(2p) and Ge(3d) core levels induced by metal adatoms on silicon and germanium surfaces, respectively, as a function of the difference $X_m - X_s$ in the metal and the semiconductor electronegativities in Pauling units. After [8.14]

on silicon and germanium surfaces as a function of the difference $X_m - X_s$ between the Pauling atomic electronegativity of the metal and that of the semiconductor atoms. The covalent bonds between metal and substrate atoms still persist at metal–semiconductor interfaces, as ab-initio calculations [8.23] have demonstrated for the example of Al/GaAs(110) contacts. The pronounced linear correlation of the data displayed in Fig. 8.9 thus justifies the application of *Pauling's* electronegativity concept to semiconductor interfaces.

The combination of the physical IFIGS and the chemical electronegativity concept yields the barrier heights of ideal p-type Schottky contacts and the valence-band offsets of ideal semiconductor heterostructures as

$$\Phi_{Bp} = \Phi_{bp}^p - S_X(X_m - X_s) \tag{8.11}$$

and

$$\Delta W_v = \Phi_{bpr}^p - \Phi_{bpl}^p + D_X(X_{sr} - X_{sl}) , \tag{8.12}$$

respectively, where $\Phi_{bp}^p = W_{bp} - W_v(\Gamma)$ is the energy distance from the valence-band maximum to the branch point of the IFIGS or the p-type branch-point energy. It has the physical meaning of a zero-charge-transfer barrier height. The slope parameters S_X and D_X are explained at the end of this section.

The IFIGS derive from the virtual gap states of the complex band structure of the semiconductor. Their branch point is an average property of the semiconductor. *Tersoff* [8.24, 27] calculated the branch-point energies Φ_{bp}^p of Si, Ge, and 13 of the III–V and II–VI compound semiconductors. He used a linearized augmented plane-wave method and the local density approximation. Such extensive computations may be avoided. *Mönch* [8.28] applied *Baldereschi's* concept [8.29] of mean-value k-points to calculate the branch-point energies of zincblende-structure compound semiconductors. He first demonstrated that the quasi-particle band gaps of diamond, silicon, germanium, 3C-SiC, GaAs and CdS at the mean-value k-point equal their average or dielectric band gaps [8.30]

$$W_{dg} = \hbar\omega_p / \sqrt{\varepsilon_\infty - 1} , \tag{8.13}$$

where $\hbar\omega_p$ is the plasmon energy of the bulk valence electrons. *Mönch* then used *Tersoff's* Φ_{bp}^p values, calculated the energy dispersion $W_v(\Gamma) - W_v(\underline{k}_{mv})$ of the topmost valence band in the empirical tight-binding approximation (ETB), and plotted the resulting branch-point energies $W_{bp} - W_v(\underline{k}_{mv}) = \Phi_{bp}^p + [W_v(\Gamma) - W_v(\underline{k}_{mv})]_{ETB}$ at the mean-value k-point $\underline{k}_{mv}$ versus the widths of the dielectric band gaps W_{dg}. The linear least-squares

Table 8.1 Optical dielectric constants, widths of the dielectric band gap, and branch-point energies of diamond-, zincblende- and chalcopyrite-structure semiconductors and of some insulators

Semiconductor	ε_∞	W_{dg}(eV)	Φ_{bp}^p(eV)
C	5.70	14.40	1.77
Si	11.90	5.04	0.36[a]
Ge	16.20	4.02	0.18[a]
3C-SiC	6.38	9.84	1.44
3C-AlN	4.84	11.92	2.97
AlP	7.54	6.45	1.13
AlAs	8.16	5.81	0.92
AlSb	10.24	4.51	0.53
3C-GaN	5.80	10.80	2.37
GaP	9.11	5.81	0.83
GaAs	10.90	4.97	0.52
GaSb	14.44	3.8	0.16
3C-InN	–	6.48	1.51
InP	9.61	5.04	0.86
InAs	12.25	4.20	0.50
InSb	15.68	3.33	0.22
2H-ZnO	3.72	12.94	3.04[b]
ZnS	5.14	8.12	2.05
ZnSe	5.70	7.06	1.48
ZnTe	7.28	5.55	1.00
CdS	5.27	7.06	1.93
CdSe	6.10	6.16	1.53
CdTe	7.21	5.11	1.12
CuGaS$_2$	6.15	7.46	1.43
CuInS$_2$	6.3*	7.02	1.47
CuAlSe$_2$	6.3*	6.85	1.25
CuGaSe$_2$	7.3*	6.29	0.93
CuInSe$_2$	9.00	5.34	0.75
CuGaTe$_2$	8.0*	5.39	0.61
CuInTe$_2$	9.20	4.78	0.55
AgGaSe$_2$	6.80	5.96	1.09
AgInSe$_2$	7.20	5.60	1.11
SiO$_2$	2.10		3.99[c]
Si$_3$N$_4$	3.80		1.93[c]
Al$_2$O$_3$	3.13		3.23[c]
ZrO$_2$	4.84		≈ 3.2[c]
HfO$_2$	4.00		2.62[c]

$*\varepsilon_\infty = n^2$, [a][8.24], [b][8.25], [c][8.26]

fit to the data of the zincblende-structure compound semiconductors [8.28]

$$\Phi_{bp}^p = 0.449 \cdot W_{dg} - [W_v(\Gamma) - W_v(\underline{k}_{mv})]_{ETB} , \tag{8.14}$$

indicates that the branch points of these semiconductors lie 5% below the middle of the energy gap at the mean-value k-point. Table 8.1 displays the p-type branch-point energies of the Group IV elemental semiconductors, of SiC, and of III–V and II–VI compound semiconductors, as well as of some insulators.

A simple phenomenological model of Schottky contacts with a continuum of interface states and a constant density of states D_{is} across the semiconductor band gap yields the slope parameter [8.31, 32]

$$S_X = A_X / \left[1 + \left(e_0^2 / \varepsilon_i \varepsilon_0 \right) D_{is} \delta_{is} \right] , \tag{8.15}$$

where ε_i is an interface dielectric constant. The parameter A_X depends on the electronegativity scale chosen and amounts to $0.86\,\text{eV/Miedema-unit}$ and $1.79\,\text{eV/Pauling-unit}$. For $D_{is} \to 0$, relation (8.15) yields $S_X \to 1$ or, in other words, if no interface-induced gap states were present at the metal–semiconductor interfaces one would obtain the Schottky–Mott rule. The extension δ_{is} of the interface states may be approximated by their charge decay length $1/2q_{is}$. *Mönch* [8.32] used theoretical D_{gs}^{mi} and q_{gs}^{mi} data for metal-induced gap states (MIGS), as the IFIGS in Schottky contacts are traditionally called, and plotted the $(e_0^2/\varepsilon_0) D_{gs}^{mi}/2q_{gs}^{mi}$ values versus the optical susceptibility $\varepsilon_\infty - 1$. The linear least-squares fit to the data points yielded [8.32]

$$A_X / S_X - 1 = 0.1 \cdot (\varepsilon_\infty - 1)^2 , \tag{8.16}$$

where the reasonable assumption $\varepsilon_i \approx 3$ was made.

To a first approximation, the slope parameter D_X of heterostructure band offsets may be equated with the slope parameter S_X of Schottky contacts, since the IFIGS determine the intrinsic electric-dipole contributions to both the valence-band offsets and the barrier heights. Furthermore, the Group IV semiconductors and the elements constituting the III–V and II–VI compound semiconductors are all placed in the center columns of the Periodic Table and their electronegativities thus only differ by up to 10%. Consequently, the electric-dipole term $D_X \cdot (X_{sr} - X_{sl})$ may be neglected [8.9], so that (8.12) reduces to

$$\Delta W_v \cong \Phi_{bpr}^p - \Phi_{bpl}^p \tag{8.17}$$

for practical purposes.

8.3 Comparison of Experiment and Theory

8.3.1 Barrier Heights of Schottky Contacts

Experimental barrier heights of intimate, abrupt, clean and (above all) laterally homogeneous Schottky contacts on n-Si and n-GaAs as well as n-GaN, and the three SiC polytypes $3C$, $6H$ and $4H$ are plotted in Figs. 8.10 and 8.11, respectively, versus the difference in the Miedema electronegativities of the metals and the semiconductors. *Miedema's* electronegativities [8.33, 34] are preferred since they were derived from properties of metal alloys and intermetallic compounds, while *Pauling* [8.8] considered covalent bonds in small molecules. The p- and n-type branch-point energies, $\Phi_{bp}^p = W_{bp} - W_v(\Gamma)$ and $\Phi_{bp}^n = W_c - W_{bp}$, respectively, add up to the fundamental band-gap energy $W_g = W_c - W_v(\Gamma)$. Hence, the barrier heights of n-type Schottky contacts are

$$\Phi_{Bn}^{hom} = \Phi_{bp}^n + S_X(X_m - X_s) . \tag{8.18}$$

The electronegativity of a compound is taken as the geometric mean of the electronegativities of its constituent atoms.

First off all, the experimental data plotted in Figs. 8.10 and 8.11 clearly demonstrate that the different experimental techniques, I/V, BEEM, IPEYS and PES, yield barrier heights of laterally homogeneous Schottky contacts which agree within the margins of experimental error.

Second, all experimental data are quantitatively explained by the branch-point energies (8.14) and the slope parameters (8.16) of the IFIGS-and-electronegativity theory. As was already mentioned in Sect. 8.1.1, the stacking fault, which is part of the interfacial Si(111)-$(7 \times 7)^i$ reconstruction, causes an *extrinsic* electric dipole in addition to the *intrinsic* IFIGS electric dipole. The latter one is present irrespective of whether the interface structure is reconstructed or $(1 \times 1)^i$-unreconstructed. The extrinsic stacking fault-induced electric dipole quantitatively explains the experimentally observed barrier height lowering of $76 \pm 2\,\text{meV}$.

Third, the IFIGS lines in Figs. 8.11a and 8.11b were drawn using the branch-point energies calculated for *cubic* $3C$-GaN and $3C$-SiC, respectively, since relation (8.12) was derived for zincblende-structure compounds only. However, the Schottky contacts were prepared on wurtzite-structure $2H$-GaN and not just on cubic $3C$-SiC but also on its hexagonal polytypes $4H$ and $6H$. The good agreement between the experimen-
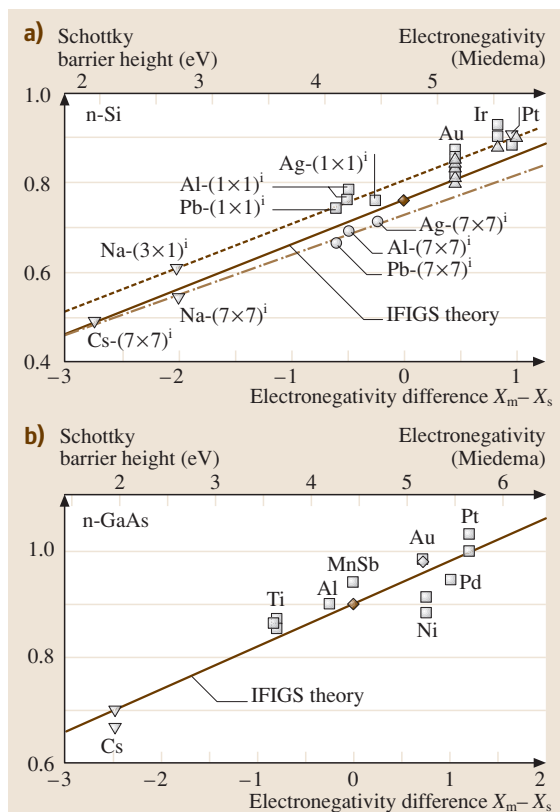
Fig. 8.10a,b Barrier heights of laterally homogeneous n-type silicon (**a**) and GaAs Schottky contacts (**b**) versus the difference in the Miedema electronegativities of the metals and the semiconductors. The ⊙ and □, ◇, △, and ▽ symbols differentiate the data from I/V, BEEM, IPEYS, and PES measurements, respectively. The *dashed* and the *dash-dotted lines* are the linear least-squares fits to the data from diodes with $(1 \times 1)^i$-unreconstructed and $(7 \times 7)^i$-reconstructed interfaces, respectively. The *solid* IFIGS *lines* are drawn with $S_X = 0.101$ eV/Miedema-unit and $\Phi_{bp}^p = 0.36$ eV for silicon (**a**) and with $S_X = 0.08$ eV/Miedema-unit and $\Phi_{bp}^p = 0.5$ eV for GaAs (**b**). After [8.14]

tal data and the IFIGS lines indicates that the p-type branch-point energies are rather insensitive to the specific bulk lattice structure of the semiconductor. This conclusion is further justified by the band-edge discontinuities of the semiconductor heterostructures, which were experimentally observed and are discussed in Sect. 8.3.2, and by the band-edge offsets of $3C/2H$ homostructures that were calculated for various semiconductors [8.35–39].
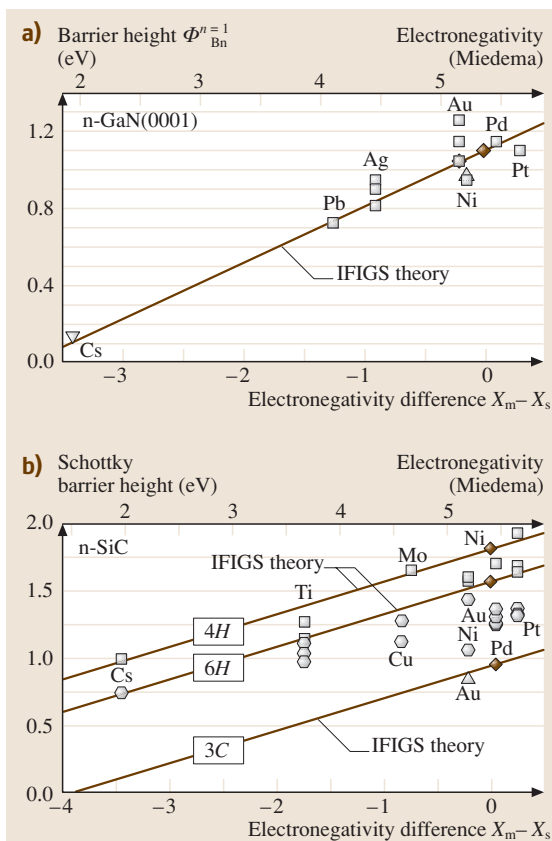

Fig. 8.11a,b Barrier heights of laterally homogeneous n-type GaN(0001) (**a**) and $3C$-, $4H$-, and $6H$-SiC Schottky contacts (**b**) versus the difference in the Miedema electronegativities of the metals and the semiconductors. (**a**): The □ ◇, △, and ▽ symbols differentiate the data from I/V, BEEM, IPEYS, and PES measurements, respectively. The *solid* IFIGS *line* is drawn with $S_X = 0.29$ eV/Miedema-unit and $\Phi_{bp}^p = 2.37$ eV. (**b**): The □, ◇, and ⊙ *symbols* differentiate data of $4H$-, $6H$- and $3C$-SiC Schottky contacts, respectively. The *solid* IFIGS *lines* are drawn with the band gaps of the polytypes minus $\Phi_{bp}^p = 1.44$ eV of cubic $3C$-SiC and $S_X = 0.24$ eV/Miedema-unit. After [8.14]

8.3.2 Band Offsets of Semiconductor Heterostructures

In the bulk, and at interfaces of sp^3-coordinated semiconductors, the chemical bonds are covalent. The simplest semiconductor–semiconductor interfaces are *lattice-matched* heterostructures. However, if the bond lengths of the two semiconductors differ then the interface will respond with tetragonal lattice distortions. Such
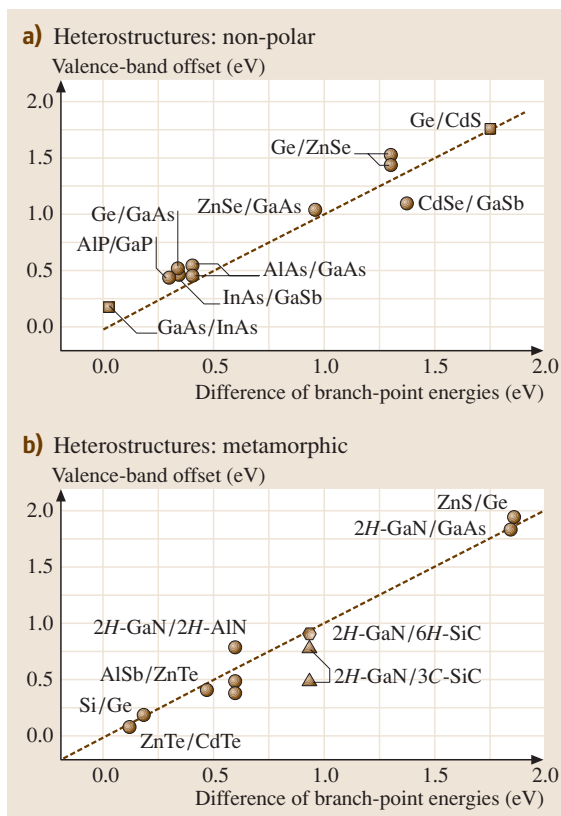
a) Heterostructures: non-polar

Valence-band offset (eV)

b) Heterostructures: metamorphic

Valence-band offset (eV)

Fig. 8.12a,b Valence band offsets at nonpolar (110)-oriented **(a)** and metamorphic semiconductor heterostructures **(b)** versus the difference between the p-type branch-point energies of the semiconductors in contact. After [8.14]

pseudomorphic interfaces are under tensile or compressive stress. If the strain energy becomes too large then it is energetically more favorable to release the stress by the formation of misfit dislocations. Such *metamorphic* interfaces are almost relaxed.

In contrast to isovalent heterostructures, the chemical bonds at heterovalent interfaces require special attention, since interfacial donor- and acceptor-type bonds may cause interfacial electric dipoles [8.40]. No such extrinsic electric dipoles will exist normal to nonpolar (110) interfaces. However, polar (001) interfaces behave quite differently. Acceptor bonds or donor bonds normal to the interface would exist at abrupt heterostructures. But, for reasons of charge neutrality, they have to be compensated by a corresponding density of donor bonds and acceptor bonds, respectively. This may be achieved by an intermixing at the interface which, on

the other hand, causes extrinsic electric dipoles. Their components normal to the interface will add an extrinsic electric-dipole contribution to the valence-band offset. In the following, only nonpolar, lattice-matched isovalent, and metamorphic heterostructures will be discussed.

The valence-band offsets at nonpolar, in other words (110)-oriented, heterostructures of compound semiconductors should equal the difference in the branch-point energies of the two semiconductors in contact provided the intrinsic IFIGS electric-dipole contribution can be neglected, see relation (8.17). Figure 8.12a displays respective experimental results for diamond- and zincblende-structure semiconductors as a function of the difference in the branch-point energies given in Table 8.1. The dashed line clearly demonstrates that the experimental data are execellently explained by the theoretical branch-point energies or, in other words, by the IFIGS theory.

As an example of lattice-matched and isovalent heterostructures, Fig. 8.13 shows valence-band offsets for $Al_{1-x}Ga_xAs/GaAs$ heterostructures as a function of the alloy composition x. The IFIGS branch-point energies of the alloys were calculated assuming virtual $Al_{1-x}Ga_x$ cations [8.28], and were found to vary linearly as a function of composition between the values of AlAs and GaAs. More refined first-principles calculations yielded identical results [8.41, 42]. Figure 8.13 reveals that the theoretical IFIGS valence-band offsets fit the experimental data excellently.

Figure 8.12b displays valence-band offsets for metamorphic heterostructures versus the difference in the branch-point energies of the two semiconductors. The
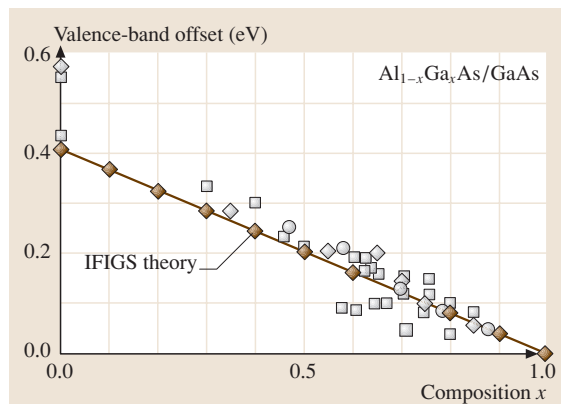

Valence-band offset (eV)

Fig. 8.13 Valence band offsets of lattice-matched and isovalent $Al_{1-x}Ga_xAs/GaAs$ heterostructures as a function of alloy composition x. After [8.14]

dashed line indicates that the experimental results are again excellently described by the theoretical IFIGS data. This is true not only for heterostructures between cubic zincblende- and hexagonal wurtzite-structure compounds but also for wurtzite-structure Group III nitrides grown on both cubic 3*C*- and hexagonal 6*H*-SiC substrates. These observations suggest the following conclusions. First, all of the heterostructures considered in Fig. 8.12b are only slightly (if at all) strained, although their lattice parameters differ by up to 19.8%. Second, the calculations of the IFIGS branch-point energies assumed zincblende-structure semiconductors. These values, on the other hand, reproduce the experimental valence band offsets irrespective of whether the semiconductors have zincblende, wurtzite or, as in the case of 6*H*-SiC, another hexagonal-polytype structure. These findings again support the conclusion drawn from the GaN and SiC Schottky barrier heights in the previous section, that the IFIGS branch-point energies are rather insensitive to the specific semiconductor bulk lattice structure.

8.3.3 Band–Structure Lineup at Insulator Interfaces

The continuing miniaturization of complementary metal–oxide–semiconductor (CMOS) devices requires gate insulators where the dielectric constants (κ) are larger than the value of the silicon dioxide conventionally used. At present, the high-κ insulators Al_2O_3, ZrO_2, and HfO_2 are being intensively studied. Insulators may be considered to be wide-gap semiconductors. Hence, relations (8.11) and (8.12) also apply to insulator Schottky contacts and heterostructures. Unfortunately, the branch-point energies of these insulators cannot be obtained from relation (8.14) since it is valid for zincblende-structure compound semiconductors only. However, the experimental band offsets reported for SiO_2, Si_3N_4, Al_2O_3, and HfO_2 heterostructures may be plotted as a function of the branch-point energies of the respective semiconductors [8.26]. Figure 8.14a reveals that the valence-band offsets become smaller with increasing branch-point energy of the semiconductors. Moreover, the data points reported for the many different SiO_2 heterostructures studied indicate a linear dependence for the valence-band offsets on the branch-point energy of the semiconductors, which may be written as

$$\Delta W_v = \varphi_{vbo} \left[\Phi_{bp}^p(\text{ins}) - \Phi_{bp}^p(\text{sem}) \right] , \qquad (8.19)$$

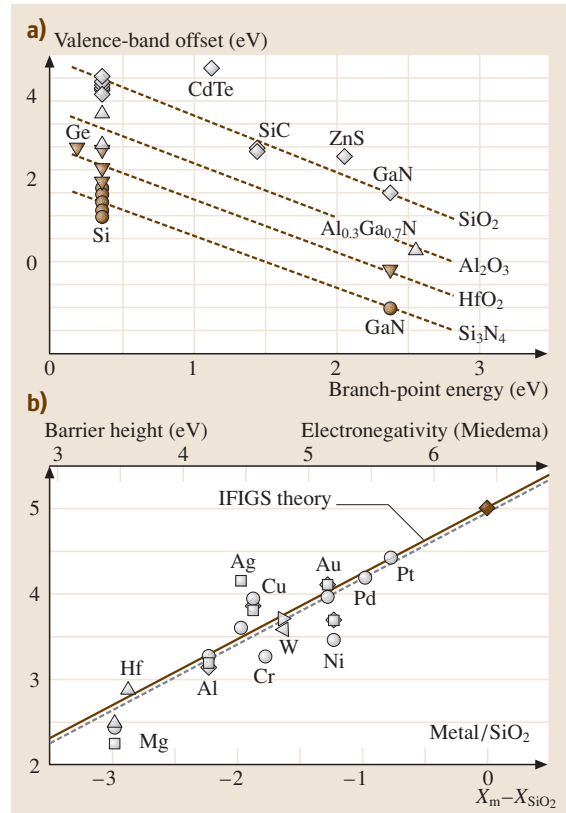since the valence band offsets of insulator homostructures will definitely vanish. Such a linear relationship

Fig. 8.14 (a) Valence band offsets of SiO_2, Si_3N_4, Al_2O_3 and HfO_2 heterostructures versus the p-type branch-point energies of the respective semiconductors. **(b)** n-type barrier heights of SiO_2 Schottky contacts versus the difference between electronegativities of the metal and SiO_2. The *dashed line* is the linear least-squares fit to the data points. The *solid* IFIGS *line* is drawn with $\Phi_{bp}^n = 5$ eV ($W_g = 9$ eV) and $S_X = 0.77$ eV/Miedema-unit ($\varepsilon_\infty = 2.1$). After [8.25]

can also be adopted for the Al_2O_3, HfO_2 and Si_3N_4 heterostructures, where less experimental results are available. Hence, the data displayed in Fig. 8.14a provide a means of determining the branch-point energies $\Phi_{bp}^p(\text{ins})$ of SiO_2, Si_3N_4, and the high-κ oxides Al_2O_3 and HfO_2. The dashed lines in Fig. 8.14a are the linear least-squares fits to the respective data points. The experimental slope parameters φ_{vbo} range from 1.16 to 1.23 for HfO_2 and SiO_2 heterostructures, respectively, while relation (8.12) predicts $\varphi_{vbo} = 1$ provided that the electric dipole term $D_X \cdot (X_{sr} - X_{sl})$ vanishes. However, as well-established as this simplifying assumption is for the classical semiconductor heterostructures discussed in Sect. 8.3.2, it has ques-

tionable validity for the insulators considered here since they are much more ionic. Hence, the difference $\varphi_{vbo} - 1$ may be attributed to intrinsic electric-dipole layers at these insulator–semiconductor interfaces. The p-type branch-point energies Φ_{bp}^{p} of the insulators obtained from the linear least-squares fits are displayed in Table 8.1.

The reliability of these branch-point energies may be checked by, for example, analyzing barrier heights of respective insulator Schottky contacts. Such data are only available for SiO_2. Figure 8.14b displays the barrier heights of SiO_2 Schottky contacts as a function of the electronegativity difference $X_m - X_{SiO_2}$, where the electronegativity of SiO_2 is estimated as 6.42 Miedema-units. The linear least-squares fit

$$\Phi_{Bn} = (4.95 \pm 0.19) + (0.77 \pm 0.10)$$
$$\times (X_m - X_{SiO_2})[eV] \tag{8.20}$$

to the experimental data agrees excellently with the prediction from the IFIGS-and-electronegativity theory.

8.4 Final Remarks

The local density approximation to density functional theory (LDA-DFT) is the most powerful and widely used tool in theoretical studies of the ground-state properties of solids. However, excitation energies such as the width of the energy gaps between the valence and conduction bands of semiconductors cannot be correctly obtained from such calculations. The fundamental band gaps of the elemental semiconductors C, Si and Ge as well as of the III–V and II–VI compounds are notoriously underestimated by 25 to 50%. However, it became possible to compute quasi-particle energies and band gaps of semiconductors from first principles using the so-called GW approximation for the electron self-energy [8.43, 44]. The resulting band gap energies agree to within 0.1 to 0.3 eV with experimental values.

For some specific metal–semiconductor contacts, the band-structure lineup was also studied by state-of-the-art ab-initio LDA-DFT calculations. The resulting LDA-DFT barrier heights were then subjected to a-posteriori corrections which consider quasi-particle effects and, if necessary, spin-orbit interactions and semicore-orbital effects. However, comparison of the theoretical results with experimental data gives an inconsistent picture. The *mean* values of the barrier heights of Al- and Zn/p-ZnSe contacts, which were calculated for different interface configurations using ab-initio LDA-DF theory and a-posteriori spin-orbit and quasi-particle corrections [8.45, 46], agree with the experimental data to within the margins of experimental error. The same conclusion was reached for Al/$Al_{1-x}Ga_xAs$ Schottky contacts [8.47]. However, ab-initio LDA-DFT barrier heights of Al-, Ag-, and Au/p-GaN contacts [8.48,49], as well as of Al- and Ti/3C-SiC(001) interfaces [8.50,51], strongly deviate from the experimental results.

As already mentioned, ab-initio LDF-DFT valenc band offsets of $Al_{1-x}Ga_xAs$/GaAs heterostructures [8.41, 42] reproduce the experimental results well. The same holds for *mean* values of LDF-DFT valence-band offsets computed for different interface configurations of GaN- and AlN/SiC heterostructures [8.52–56].

The main difficulty which the otherwise extremely successful ab-initio LDF-DFT calculations encounter when describing semiconductor interfaces is not the precise exchange-correlation potential, which may be estimated in the GW approximation, but their remarkable sensitivity to the geometrical and compositional structure right at the interface. This aspect is more serious at metal–semiconductor interfaces than at heterostructures between two sp^3-bonded semiconductors. The more conceptual IFIGS-and-electronegativity theory, on the other hand, quantitatively explains not only the barrier heights of ideal Schottky contacts but also the valence-band offsets of semiconductor heterostructures. Here again, the Schottky contacts are the more important case, since their zero-charge-transfer barrier heights equal the branch-point energies of the semiconductors, while the valence-band offsets are determined by the differences in the branch-point energies of the semiconductors in contact.

References

8.1   W. Schottky: Naturwissenschaften **26**, 843 (1938)
8.2   F. Braun: Pogg. Ann. Physik Chemie **153**, 556 (1874)
8.3   N. F. Mott: Proc. Camb. Philos. Soc. **34**, 568 (1938)
8.4   W. Schottky: Phys. Zeitschr. **41**, 570 (1940)
8.5   J. Bardeen: Phys. Rev. **71**, 717 (1947)
8.6   V. Heine: Phys. Rev. **138**, A1689 (1965)

8.7   C. Tejedor, F. Flores: J. Phys. C **11**, L19 (1978)
8.8   L. N. Pauling: *The Nature of the Chemical Bond* (Cornell Univ. Press, Ithaca 1939)
8.9   W. Mönch: On the Present Understanding of Schottky Contacts. In: *Festkörperprobleme*, Vol. 26, ed. by P. Grosse (Vieweg, Braunschweig 1986) p. 67
8.10   W. Mönch: Phys. Rev. B **37**, 7129 (1988)
8.11   R. Schmitsdorf, T. U. Kampen, W. Mönch: Surf. Sci. **324**, 249 (1995)
8.12   J. L. Freeouf, T. N. Jackson, S. E. Laux, J. M. Woodall: Appl. Phys. Lett. **40**, 634 (1982)
8.13   W. Schottky: Phys. Zeitschr. **15**, 872 (1914)
8.14   W. Mönch: *Electronic Properties of Semiconductor Interfaces* (Springer, Berlin, Heidelberg 2004)
8.15   H.A. Bethe: MIT Radiation Lab. Rep. 43–12 (1942)
8.16   K. Takayanagi, Y. Tanishiro, M. Takahashi, S. Takahashi: Surf. Sci. **164**, 367 (1985)
8.17   H.–J. Im, Y. Ding, J. P. Pelz, W. J. Choyke: Phys. Rev. B **64**, 075310 (2001)
8.18   W. J. Kaiser, L. D. Bell: Phys. Rev. Lett. **60**, 1406 (1988)
8.19   L. D. Bell, W. J. Kaiser: Phys. Rev. Lett. **61**, 2368 (1988)
8.20   R. Turan, B. Aslan, O. Nur, M. Y. A. Yousif, M. Willander: Appl. Phys. A **72**, 587 (2001)
8.21   J. Cohen, J. Vilms, R.J. Archer: Hewlett–Packard R&D Report AFCRL–69–0287 (1969)
8.22   R. W. Grant, J. R. Waldrop, E. A. Kraut: Phys. Rev. Lett. **40**, 656 (1978)
8.23   S. B. Zhang, M. L. Cohen, S. G. Louie: Phys. Rev. B **34**, 768 (1986)
8.24   J. Tersoff: J. Vac. Sci. Technol. B **4**, 1066 (1986)
8.25   W. Mönch: Appl. Phys. Lett. **86**, 162101 (2005)
8.26   W. Mönch: Appl. Phys. Lett. **86**, 122101 (2005)
8.27   J. Tersoff: Phys. Rev. Lett. **52**, 465 (1984)
8.28   W. Mönch: J. Appl. Phys. **80**, 5076 (1996)
8.29   A. Baldereschi: Phys. Rev. B **7**, 5212 (1973)
8.30   D. R. Penn: Phys. Rev. **128**, 2093 (1962)
8.31   A. M. Cowley, S. M. Sze: J. Appl. Phys. **36**, 3212 (1965)
8.32   W. Mönch: Appl. Surf. Sci. **92**, 367 (1996)
8.33   A. R. Miedema, F. R. de Boer, P.F. de Châtel: J. Phys. F **3**, 1558 (1973)
8.34   A. R. Miedema, P. F. de Châtel, F. R. de Boer: Physica **100B**, 1 (1980)
8.35   A. Qteish, V. Heine, R. J. Needs: Phys. Rev. B **45**, 6534 (1992)
8.36   P. Käckell, B. Wenzien, F. Bechstedt: Phys. Rev. B **50**, 10761 (1994)
8.37   S. Ke, K. Zhang, X. Xie: J. Phys. Condens. Mat. **8**, 10209 (1996)
8.38   J. A. Majewski, P. Vogl: MRS Internet J. Nitride Semicond. Res. **3**, 21 (1998)
8.39   S.–H. Wei, S. B. Zhang: Phys. Rev. B **62**, 6944 (2000)
8.40   W. A. Harrison, E. A. Kraut, J. R. Waldrop, R. W. Grant: Phys. Rev. B **18**, 4402 (1978)
8.41   J. S. Nelson, A. F. Wright, C. Y. Fong: Phys. Rev. B **43**, 4908 (1991)
8.42   S. B. Zhang, M. L. Cohen, S. G. Louie, D. Tománek, M. S. Hybertsen: Phys. Rev. B **41**, 10058 (1990)
8.43   M. S. Hybertsen, S. G. Louie: Phys. Rev. B **34**, 5390 (1986)
8.44   R. W. Godby, M. Schlüter, L. J. Sham: Phys. Rev. B **37**, 10159 (1988)
8.45   M. Lazzarino, G. Scarel, S. Rubini, G. Bratina, L. Sorba, A. Franciosi, C. Berthod, N. Binggeli, A. Baldereschi: Phys. Rev. B **57**, R9431 (1998)
8.46   S. Rubini, E. Pellucchi, M. Lazzarino, D. Kumar, A. Franciosi, C. Berthod, N. Binggeli, A. Baldereschi: Phys. Rev. B **63**, 235307 (2001)
8.47   J. Bardi, N. Binggeli, A. Baldereschi: Phys. Rev. B **54**, R11102 (1996)
8.48   S. Picozzi, A. Continenza, G. Satta, S. Massidda, A. J. Freeman: Phys. Rev. B **61**, 16736 (2000)
8.49   S. Picozzi, G. Profeta, A. Continenza, S. Massidda, A. J. Freeman: Phys. Rev. B **65**, 165316 (2002)
8.50   J. Hoekstra, M. Kohyama: Phys. Rev. B **57**, 2334 (1998)
8.51   M. Kohyama, J. Hoekstra: Phys. Rev. B **61**, 2672 (2000)
8.52   M. Städele, A. J. Majewski, P. Vogl: Phys. Rev. B **56**, 6911 (1997)
8.53   J. A. Majewski, M. Städele, P. Vogl: Mater. Res. Soc. Symp. Proc. **449**, 917 (1997)
8.54   N. Binggeli, P. Ferrara, A. Baldereschi: Phys. Rev. B **63**, 245306 (2001)
8.55   B. K. Agrawal, S. Agrawal, R. Srivastava, P. Srivastava: Physica E **11**, 27 (2001)
8.56   M. R. Laridjani, P. Masri, J. A. Majewski: Mater. Res. Soc. Symp. Proc. **639**, G11.34 (2001)